
A NUMERICAL INVESTIGATION OF THE ENERGY
TRANSFER OF A BODY UNDER FLUIDELASTIC
GALLOPING

BY H.G.K.G JAYATUNGA

A THESIS SUBMITTED TO MONASH UNIVERSITY IN FULFILMENT OF THE REQUIREMENTS
FOR THE DEGREE OF

DOCTOR OF PHILOSOPHY

Department of Mechanical Engineering

Monash University

October 2015

CONTENTS

1	Introduction	2
1.0.1	Static body results	4
1.0.2	Formulation of the new dimensionless groups Π_1 and Π_2	5
1.0.3	Comparison of Π_1 and Π_2 with classical VIV parameters	8
1.0.4	Comparison of power between high and low Re data	8
1.0.5	Dependence on mass-stiffness, Π_1	10
1.0.6	Dependence on the mass ratio m^*	14
1.0.7	Comparison with DNS data	14
1.1	Summary of the governing parameters of fluid-elastic galloping	22

CHAPTER 1

INTRODUCTION

The review of published literature reveals that fluid-elastic galloping has a potential to be used as a mechanism for energy extraction (Barrero-Gil et al., 2010). Thus, the following questions emerged. What are the optimum parameters for energy transfer in a galloping system? How do they influence galloping?

Another fluid-structure interaction phenomenon, vortex-induced vibration (VIV), has also been investigated as a candidate for the power extraction from flows. The work from Bernitsas et al. (2008, 2009); Raghavan and Bernitsas (2011); Lee and Bernitsas (2011) and others from the same group at the University of Michigan have made significant progress with this problem. Therefore it may seem, at least initially, reasonable to present data from the fluid-elastic problem in the same parameters as typically used in VIV studies, which could be observed in current literature on galloping (Barrero-Gil et al., 2009, 2010; Parkinson and Smith, 1964).

However, the data presented in the pioneering study on energy harvesting from galloping (Barrero-Gil et al., 2010) presented using classical VIV parameters (i.e. U^* , $m^*\zeta$), shows that the mean power data does not collapse well. The reason behind this would be the difference in time-scales of VIV and galloping. Thus the work presented in this chapter is focused on testing this hypothesis and obtain the optimum conditions for mean power output.

Since the the Quasi-steady state model is the primary mathematical model used to model galloping in this study, the fluid-dynamic characteristics of flow over a static body

are presented and discussed first as it is the . Then, the natural time scales of the system are obtained using the linearised QSS model. Next, the new non-dimensional governing parameters Π_1 and Π_2 , are formulated by non-dimensionalising the QSS model from these natural time scales, followed by a comparison of galloping data using the classical VIV parameters and Π_1 and Π_2 . Then, the influence of Π_1 and Π_2 and the conditions for an optimum power output are discussed from QSS data. Finally, the QSS data are compared and discussed against FSI direct numerical simulations and final conclusions are presented.

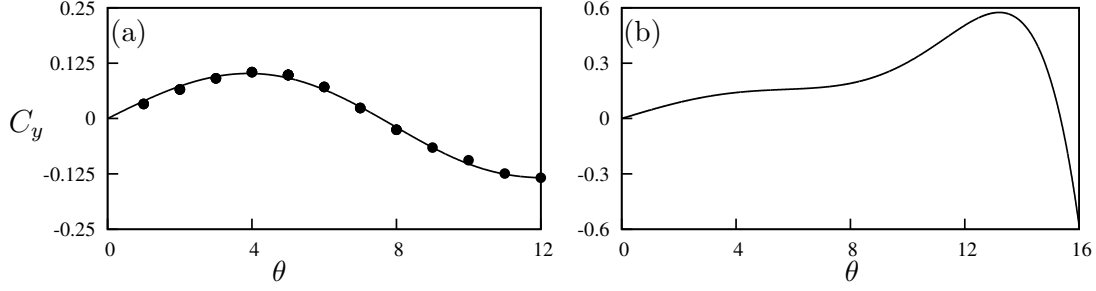


Figure 1.1: Lift coefficient, C_y , as a function of incidence angle θ , for a static square cross section. (a) Data from simulations at $Re = 200$ and (b) data from Parkinson and Smith (1964) at $Re = 22300$. The values at points (\bullet) are acquired from direct numerical simulations. Curves in both plots are 7th-order interpolating polynomials used to interpolate the fluid forcing for the QSS model.

1.0.1 Static body results

The main data acquisition tool for galloping is the QSS model. As discussed in chapter , the QSS model uses an interpolation polynomial of the static body lift data as the driving force of the QSS equation. These static body data and the polynomial data are presented here. Figure 1.1 shows the plots of time averaged C_y data as a function of θ , as well as the interpolation polynomial curves. Data are acquired for high and low Reynolds numbers. For high Reynolds numbers, the static body polynomial data are obtained from Parkinson and Smith (1964) while for low Reynolds numbers a 7th order non-linear least square regression fit on static body DNS simulations were used. The coefficients of these polynomials are presented in table 1.1.

There are several differences that can be observed between high and low Reynolds number data. The peak value of C_y is significantly lower at $Re = 200$ ($C_y = 0.12$ at 5°) compared to $Re = 22300$ ($C_y = 0.57$ at 13°). The inflection point present around 8° for $Re = 22300$ is not present at $Re = 200$. This agrees with the findings of Luo et al. (2003). Luo et al. (2003) concluded that hysteresis in the system response occurs due to the inflection point in the C_y curve. Therefore, hysteresis could not be observed at $Re = 200$.

The range of incident flow angles where C_y remains positive is narrow at $Re = 200$ ($0^\circ < \theta \leq 7^\circ$) compared to $Re = 22300$ ($0^\circ < \theta \leq 15^\circ$). This positive range sustains galloping, as the power is only transferred from the fluid to the supporting structure within

Case	a_1	a_3	a_5	a_7
$Re = 200$	2.32	197.8	4301.7	30311.9
$Re = 22300$	2.69	168	1670	59900

Table 1.1: Coefficient values used in the 7th order interpolation polynomial for high ($Re = 22300$) and low ($Re = 200$) Reynolds numbers. These data are used as input data to calculate the right-hand side of Eq. ?? throughout this study.

this range of incident angles. This is because the fluid forces are acting in the direction of velocity of the body, or in phase with, the oscillating body as demonstrated by equation ?. Incident angles beyond this range suppress the galloping as power is transferred in the opposite direction, i.e; from body to fluid. Thus, it is expected that the transferred power at $Re = 200$ to be significantly lower than at $Re = 22300$, because of the relative low values of C_y and the narrow range of positive C_y at $Re = 200$.

1.0.2 Formulation of the new dimensionless groups Π_1 and Π_2

The natural time scales of the system can be found by solving for the eigenvalues of the linearised equation of motion (Eq:??), namely

$$m\ddot{y} + c\dot{y} + ky = \frac{1}{2}\rho U^2 \mathcal{A}a_1 \left(\frac{\dot{y}}{U} \right), \quad (1.1)$$

which is a simplified version of the equation of motion presented in equation ?? with the polynomial series for the lift force truncated at the linear term.

Combining the \dot{y} terms and solving for eigenvalues gives

$$\lambda_{1,2} = -\frac{1}{2} \frac{c - \frac{1}{2}\rho U \mathcal{A}a_1}{m} \pm \frac{1}{2} \sqrt{\left[\frac{c - \frac{1}{2}\rho U \mathcal{A}a_1}{m} \right]^2 - 4 \frac{k}{m}}. \quad (1.2)$$

If it is assumed that the spring is relatively weak, $k \rightarrow 0$, a single non-zero eigenvalue remains. This eigenvalue is

$$\lambda = -\frac{c - \frac{1}{2}\rho U \mathcal{A}a_1}{m}. \quad (1.3)$$

1. INTRODUCTION

Further, if it is assumed that the mechanical damping is significantly weaker than the fluid-dynamic forces on the body, $c \rightarrow 0$ and

$$\lambda = \frac{\frac{1}{2}\rho U \mathcal{A} a_1}{m}. \quad (1.4)$$

In this form, λ represents the inverse time scale of the motion of the body due to the effect of the long-time fluid-dynamic forces. In fact, the terms can be regrouped and λ written as

$$\lambda = \frac{a_1}{m^*} \frac{U}{D} \quad (1.5)$$

Written this way, the important parameters that dictate this inverse time scale are clear. The rate of change in the fluid-dynamic force with respect to angle of attack when the body is at the equilibrium position, $\partial C_y / \partial \alpha$, is represented by a_1 . The mass ratio is represented by m^* . The inverse advective time scale of the incoming flow is represented by the ratio U/D . Increasing a_1 would mean the force on the body would increase more rapidly with small changes in the angle of attack, θ , or transverse velocity. Equation 1.5 shows that such a change will increase the inverse time scale, or analogously decrease the response time of the body. Increasing the mass of the body, thereby increasing m^* , has the opposite effect. The inverse time scale is decreased, or as might be expected, a heavier body will respond more slowly.

This timescale can then be used to non-dimensionalize the equation of motion, and to find the relevant dimensionless groups of the problem. It was suggested by Shiels et al. (2001); Leonard and Roshko (2001) to use a flow-based timescale such D/U for the characteristic time for flow-induced vibration problems, rather than a structural-based timescale such as the natural frequency. This point is discussed further in ?. Here, this advective time is further scaled by the mass ratio m^* , as suggested from the eigenvalues of the linearized equation of motion. Hence, if the non-dimensional time, τ , is defined such that $\tau = t(a_1/m^*)(U/D)$, the equation of motion presented in equation ?? can be non-dimensionalized as

$$\ddot{Y} + \frac{m^*}{a_1^2} \frac{k D^2}{m U^2} Y = \left(\frac{1}{2} - \frac{m^*}{a_1} \frac{c D}{m U} \right) \dot{Y} - \frac{a_1 a_3}{m^*{}^2} \dot{Y}^3 + \frac{a_1^3 a_5}{m^*{}^4} \dot{Y}^5 - \frac{a_1^5 a_7}{m^*{}^6} \dot{Y}^7. \quad (1.6)$$

The coefficients can be regrouped into combinations of non-dimensional groups, and

rewritten as

$$\ddot{Y} + \frac{4\pi^2 m^{*2}}{U^{*2} a_1^2} Y = \left(\frac{1}{2} - \frac{c^* m^*}{a_1} \right) \dot{Y} - \frac{a_1 a_3}{m^{*2}} \dot{Y}^3 + \frac{a_1^3 a_5}{m^{*4}} \dot{Y}^5 - \frac{a_1^5 a_7}{m^{*6}} \dot{Y}^7, \quad (1.7)$$

where U^* is the reduced velocity typically used as an independent variable in vortex-induced vibration studies and $c^* = cD/mU$ is a non-dimensional damping parameter.

Equation 1.7 shows there are five non-dimensional parameters that play a role in setting the response of the system. These are the stiffness (represented by the reduced velocity U^*), the damping c^* , the mass ratio m^* , and the geometry and Re , represented by the coefficients of the polynomial fit to the C_y curve, a_n . The grouping of these parameters into two groups in equation 1.7 which arise by non-dimensionalising using the natural time scale of the galloping system, suggests there are two groups besides geometry (represented by a_n) and Re that dictate the response: $\Gamma_1 = 4\pi^2 m^{*2}/U^{*2} a_1^2$ and $\Gamma_2 = c^* m^*/a_1$. For a given geometry and Reynolds number, Γ_1 can be thought of as a combined mass-stiffness, whereas Γ_2 can be thought of a combined mass-damping parameter. It is assumed that during galloping the stiffness plays only a minor role because, galloping time periods are significantly large which implies that $k \rightarrow 0$. Therefore, Γ_2 seems a likely parameter to collapse the data. In fact, in the classic paper on galloping from Parkinson and Smith (1964), galloping data from wind tunnel tests is presented in terms of a parameter that can be shown to be the same as Γ_2 .

All of the quantities that make up Γ_1 and Γ_2 can, in theory, be known before an experiment is conducted. However, the quantity a_1 is a relatively difficult one to determine, requiring static body experiments or simulations. Here, the geometry is unchanged and results are only being compared at the same Re . Hence, suitable parameters can be formed by multiplying Γ_1 and Γ_2 by a_1^2 and a_1 respectively, to arrive at a mass-stiffness parameter $\Pi_1 = 4\pi^2 m^{*2}/U^{*2}$, and a mass-damping parameter defined as $\Pi_2 = c^* m^*$.

Equation 1.7 can be re-written explicitly in terms of Π_1 and Π_2 to give

$$\ddot{Y} + \Pi_1 Y = \Pi_2 \dot{Y} - \frac{a_1 a_3}{m^{*2}} \dot{Y}^3 + \frac{a_1^3 a_5}{m^{*4}} \dot{Y}^5 - \frac{a_1^5 a_7}{m^{*6}} \dot{Y}^7. \quad (1.8)$$

1.0.3 Comparison of Π_1 and Π_2 with classical VIV parameters

Figure 1.2 shows the comparison of mean power data at $Re = 200$ presented using different independent variables. Subfigures (a), (c) and (e) show the displacement amplitude, velocity amplitude and the mean power as a function of the classic VIV parameter, U^* for various damping ratios ζ . Subfigures (b), (d) and (f) shows the same data as a function of Π_2 , for various, reasonably high values of Π_1 , as defined above in section 1.0.2. The data presented using the classical VIV parameters follows the same trends as Barrero-Gil et al. (2010). Barrero-Gil et al. (2010) and Vicente-Ludlam et al. (2014) observed that the maximum dimensionless power is achieved at two times the velocity at which the galloping starts. A similar conclusion can be drawn from the data presented here in figures 1.2. However, the data presented using the dimensionless group formulated using the natural time scales of the system shows an excellent collapse for both velocity amplitude and mean power, showing that the power is essentially dictated by Π_2 . This implies that unlike VIV which is a type of resonant phenomenon, the natural frequency of the system which is used to scale U^* , ζ and Π_1 does not have a large influence on the system behaviour in these cases.

1.0.4 Comparison of power between high and low Re data

The marked success of the collapse using Π_2 for the $Re = 200$ case, particularly of the mean power, could also be replicated for the higher Re case at $Re = 22300$. Figure 1.3 presents the mean power for high Re cases for selected values of Π_1 . It is shown that the data collapse in both cases, demonstrating the validity of using Π_2 as an independent variable.

Hysteresis could be observed for the $Re = 22300$ case. The different solutions could be obtained by manipulating the initial conditions (initial displacement) of the system. The upper branch was obtained by giving an initial displacement which was higher than the expected amplitude while the lower branch was obtained by providing a lower initial displacement than the expected amplitude. Although theory shows a possible third state, it is an unstable branch which could not be achieved with a time integration method such as that employed in this study. This was also observed by Vio et al. (2007).

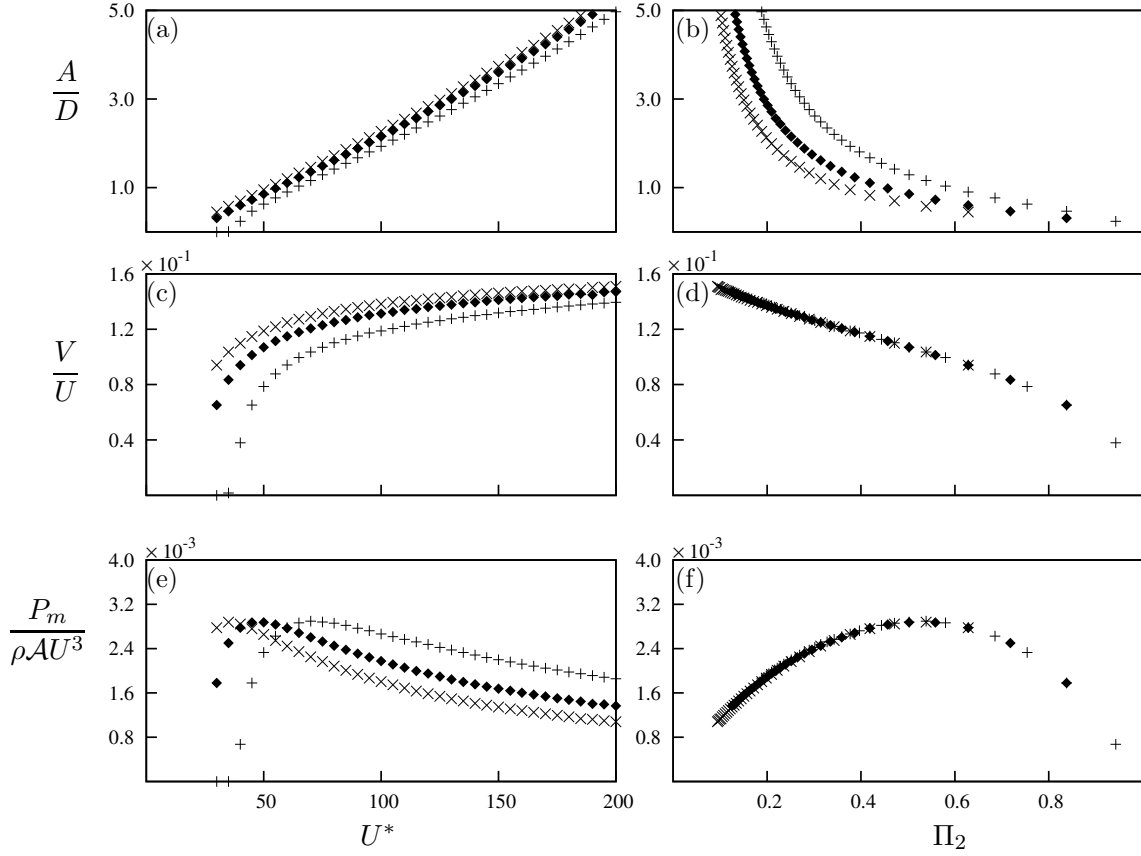


Figure 1.2: Displacement amplitude, velocity amplitude and dimensionless mean power data as functions of two different independent variables. Data presented in (a), (c) and (e) using the classical VIV parameter U^* , obtained at $Re = 200$ and $m^* = 20$ at three different damping ratios: $\zeta = 0.075$ (\times), $\zeta = 0.1$ (\blacklozenge) and $\zeta = 0.15$ (+). (b) (d) and (f) are the same data presented using the combined mass-damping parameter (Π_2) as the independent variable. Even though Π_1 varies in the range of $0.4 \leq \Pi_1 \leq 17.5$, it is clear that the power is a function of Π_2 only.

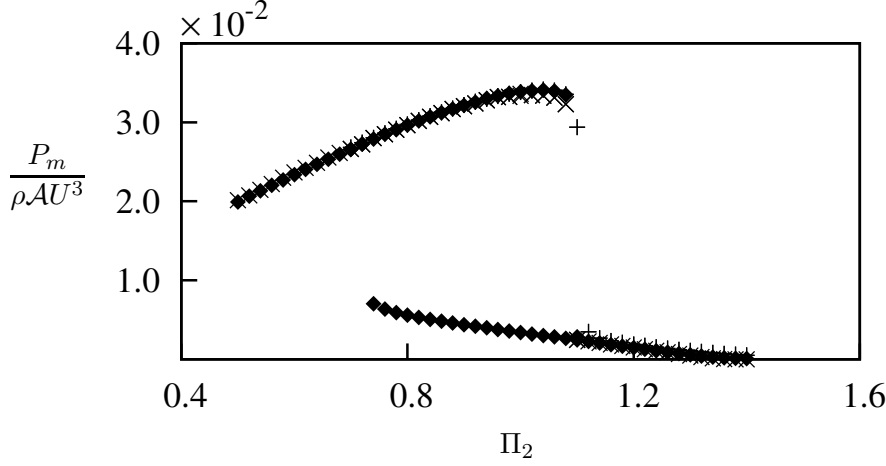


Figure 1.3: Dimensionless mean power as a function of Π_2 . Data presented at $Re = 22300$, $\Pi_1 = 200$ (\times), $\Pi_1 = 2000$ (\blacklozenge) and $\Pi_1 = 10000$ ($+$). Hysteresis could be observed at high Re .

1.0.5 Dependence on mass-stiffness, Π_1

The results of sections 1.0.3 and 1.0.4 show that the mean extracted power is essentially a function of a single variable, the combined mass-damping Π_2 . However, the timescale analysis of section 1.0.2 showed that a second variable, the combined mass-stiffness Π_1 should also play a role. Previous studies (see, for example Bouclin (1977)) have also indicated a complex interaction between the amplitude and natural frequency, particularly for high natural frequencies (or equivalently, low values of Π_1). Here, the impact of Π_1 is investigated further. Overall, the system behaviour can be separated into two wide regimes; that for “high” Π_1 and that for “low” Π_1 . These two regimes are further investigated and explained in this following section.

Figure 1.4 shows the mean power as a function of Π_2 for a range of values of Π_1 . Two subfigures are shown; subfigure (a) shows data for $\Pi_1 \geq 10$, while (b) shows data for $\Pi_1 \leq 10$. In figure 1.4(a), the collapse of the mean power is excellent, showing that for $\Pi_1 \geq 10$, the mean power is independent of Π_1 .

For low values of $\Pi_1 \leq 10$, figure 1.4(b) shows that the predicted mean power increases as Π_1 is decreased, indicating that the mean power is a weak function of Π_1 at low Π_1 levels. This provides the distinction between high and low Π_1 regimes. For high values where $\Pi_1 \geq 10$, the mean extracted power is a function of Π_2 only; for low values where

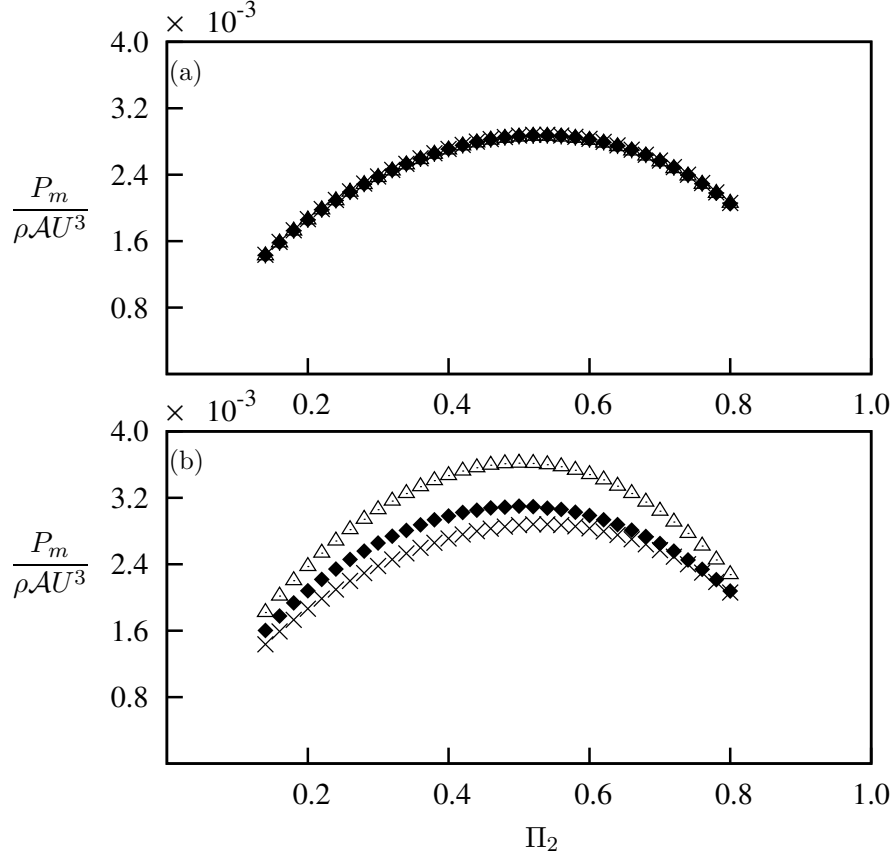


Figure 1.4: Dimensionless mean power as a function of Π_2 obtained using the QSS model at $Re = 200$. (a) High Π_1 ; data presented at four different combined mass-stiffness levels. $\Pi_1 = 10$ ($m^* = 20, U^* = 40$) (\times), $\Pi_1 = 100$ ($m^* = 80, U^* = 50$) ($+$), $\Pi_1 = 500$ ($m^* = 220, U^* = 60$) (\blacklozenge) and $\Pi_1 = 1000$ ($m^* = 400, U^* = 40$) (\triangle). (b) Low Π_1 ; data presented at $\Pi_1 = 10$ (\times), $\Pi_1 = 0.1$ (\blacklozenge), and $\Pi_1 = 0.01$ (\triangle).

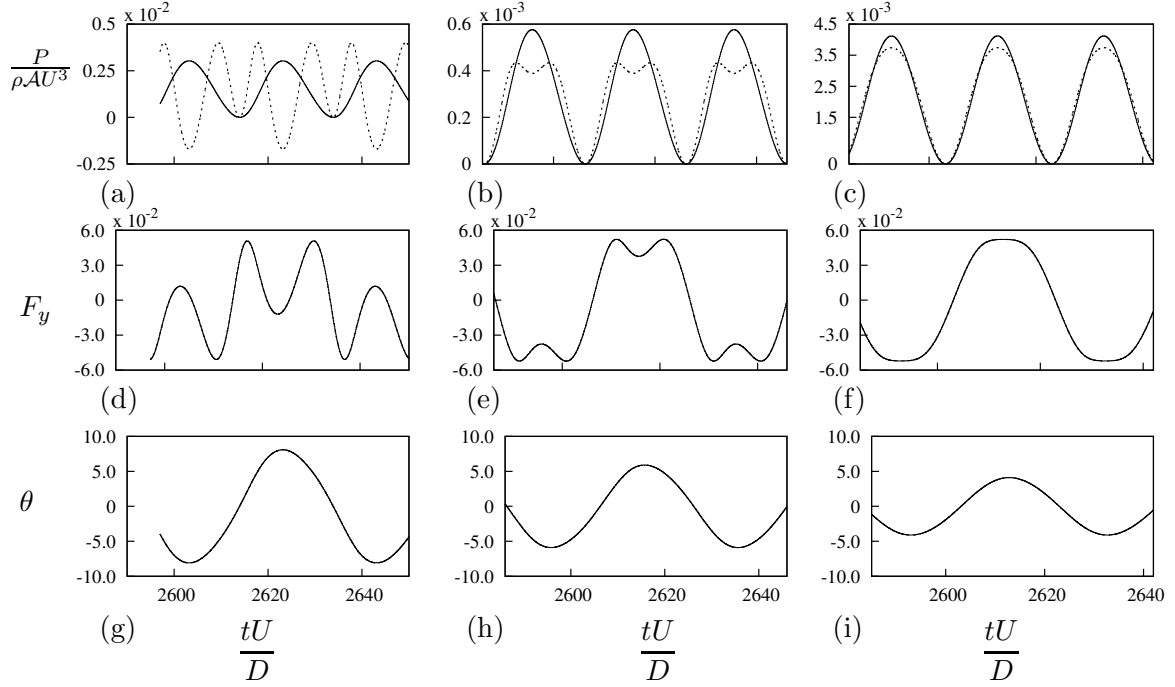


Figure 1.5: Time histories of P_t , P_d , F_y and θ at $\Pi_2 = 0.15, 0.54$ and 0.8 from the QSS model. Data was obtained at $m^* = 20$, $\Pi_1 = 10$ and $Re=200$. The time histories of P_d (—) and P_t (---) are presented for: (a) $\Pi_2 = 0.15$; (b) $\Pi_2 = 0.54$; (c) $\Pi_2 = 0.8$. Time histories of the instantaneous force F_y for: (d) $\Pi_2 = 0.15$; (e) $\Pi_2 = 0.54$; (f) $\Pi_2 = 0.8$. Time histories of the instantaneous angle θ for: (g) $\Pi_2 = 0.15$; (h) $\Pi_2 = 0.55$; (i) $\Pi_2 = 0.8$.

$\Pi_1 < 10$, the mean extracted power is a weak function of Π_1 .

Regardless of the value of Π_1 , the variation of the mean extracted power with Π_2 is essentially the same. With increasing Π_2 , the mean extracted power initially increases, before reaching some maximum value and then decreasing. This relationship between power and Π_2 can be explained by analysing the time histories of selected cases. Data at $\Pi_1 = 10$, $m^* = 20$ and $Re = 200$ are shown in figure 1.5 and are analysed as an example. Values of Π_2 less than (region 1), equal to (region 2), and greater than (region 3) the value where the mean extracted power is a maximum are analysed as examples.

The instantaneous power from the fluid to the body can be expressed as $P_t = F_y \dot{y}$. Similarly the dissipated power due to the mechanical damping can be expressed as $P_d = (c\dot{y})\dot{y}$. The time average of these two quantities, described in equations ?? and ?? must be equal due to energy conservation.

At region 1 ($\Pi_2 = 0.15$) the damping is low in comparison with region 2 and 3. While this may lead to larger oscillations, damping is required to dissipate and therefore extract power according to equation ???. Therefore, the low damping in this region leads to a low mean power output. Fig.1.5 (a) shows that P_d (the power dissipated by damping) becomes negative over some portion of the cycle. This is caused by the high velocity amplitude leading to the equivalent incident angle θ to exceed the range where C_y is positive (i.e. $0 < \theta < 6^\circ$ as shown in figure??(a)). In this portion of the cycle the fluid-dynamic force actually opposes the direction of travel and power is transferred from the structure to the fluid during those times. From an energy perspective, the mechanical damping is not sufficient to remove the energy transferred from the fluid to the structure through work during other times of the cycle because Π_2 is substantially low. Therefore this excess energy is transferred back to the fluid as depicted by the negative region of P_d .

At region 3 where $\Pi_2 = 0.8$ the damping constant is high and a clear sinusoidal signal is observed for both P_d and P_t in figure 1.5(c). Figures 1.5(f) and 1.5(i) show that equivalent incident angle θ (which for small values, is proportional to the transverse velocity of the body) is in phase with F_y . The velocity amplitude in this case is small and θ is within the range where the fluid-dynamic force increases with the incident angle (i.e. $0 < \theta \leq 5^\circ$ as shown in figure 1.1(a)). According to equation ??, these conditions are suitable for high power output. However in this case, the high damping limits the velocity amplitude and results in relatively low fluid dynamic forces.

At region 2 ($\Pi_2 = 0.54$), a balance is found between high and low values of damping. P_d is not a pure sinusoidal signal, however the signal remains periodic. From the time history graph of P_d , two ‘peaks’ are present in a single half cycle as shown in figure 1.5(b). In this case, the velocity amplitude actually exceeds the equivalent incident angle where the fluid-dynamic forces peaks (i.e. $\theta = 5^\circ$ in ?? (a)). The dips in P_d between the two peaks approximately correspond to the time where the transverse velocity is higher than 0.09 and F_y is decreasing with increasing transverse velocity. The mean power output is at its maximum. This is due to the fact that this region is the best compromise between region 1 and 3. The damping is high enough to obtain a high power output while not so high that the motion is completely suppressed.

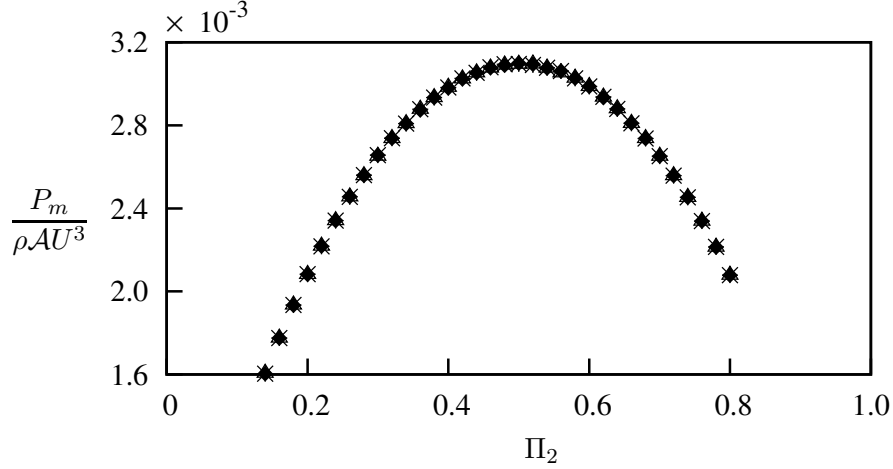


Figure 1.6: Dimensionless mean power as a function of Π_2 obtained using QSS model at $\Pi_1 = 0.1$. Data presented at $m^* = 2$ (\blacklozenge), $m^* = 20$ (\triangle) and $m^* = 50$ ($*$). The mass ratio does not have an effect on Π_1 even at low Π_1 .

1.0.6 Dependence on the mass ratio m^*

While for high values of Π_1 it is clear that the mean extracted power is a function of Π_2 only, a question arises for low values of Π_1 ; is the variation in the mean extracted power purely a function of Π_1 , or is it also a function of the mass ratio m^* ? To answer this question, the model has been solved for a fixed value of Π_1 , but for varying values of m^* . This means that Π_1 was varied by changing the system stiffness.

Figure 1.6 shows the mean extracted power as a function of Π_2 , for a fixed $\Pi_1 = 0.1$, for three different values of m^* . From the figure it is clear that the results are independent of m^* , and are a function of Π_1 and Π_2 only.

1.0.7 Comparison with DNS data

The QSS model assumes that the only force driving the system is the instantaneous lift generated by the induced velocity. However, vortex shedding is also present in this system. Therefore, an essential assumption when this model is used, is that the effect of vortex shedding is minimal. Hence, the model has been always used at high Re and at high mass ratios. This study is focused on identifying the limiting parameters of the QSS model at low Reynolds numbers by providing a comparison with DNS results.

Joly et al. (2012) showed that the displacement data obtained using the QSS assumption and DNS agree well at low Reynolds numbers, with the modification implemented to the oscillator equation which accounts for the vortex shedding. These data were obtained at zero damping levels. However, the current study is focused on the behaviour and the power transfer of the system. Therefore analysing the behaviour of the system with increasing damping is of interest.

The comparison between QSS and the DNS results is presented in figure 1.7. The maximum displacement, velocity and mean extracted power are presented as a function of Π_2 . A range of values of Π_1 are compared to the QSS model data for $\Pi_1 = 10$. Figures 1.7(a) and 1.7(b) show little variation with Π_1 , and the comparison between the QSS model and the DNS simulations is quite good. However, the mean extracted power shown in figure 1.7(c) reveals that the mean power is influenced by both Π_1 and Π_2 . This is particularly clear for low values of Π_1 , where the discrepancy between the QSS model predictions of power and the DNS simulations is the largest. Comparing figure 1.7(c) with figure 1.4(a) shows that Π_1 has much more influence on the power extracted than predicted by the QSS model for low Π_1 values. In fact, the QSS model predicts that the mean extracted power should increase with decreasing Π_1 when Π_1 moves to the low Π_1 region (figure 1.4(b)), whereas the DNS simulations show that the mean extracted power decreases with decreasing Π_1 .

Figure 1.8(a) clearly shows the dependence of the mean extracted power on Π_1 . Here, the maximum power extracted for a given value of Π_1 , over all values of Π_2 (essentially the value of extracted power at the turning point), is plotted as a function of Π_1 . These values were obtained by fitting a quadratic to the data of figure 1.6 and finding the value of mean extracted power at the turning point. The rapid decrease in the extracted power as $\Pi_1 \rightarrow 0$ is clear.

Figure 1.8(a) also shows that Π_1 is important to higher values than predicted by the QSS model. For the QSS model, the mean extracted power was essentially independent of Π_1 for $\Pi_1 > 10$, as shown by the open symbols on the figure. However, the mean extracted power from the DNS data shows a significant dependence on Π_1 for $\Pi_1 < 250$. Even so, the power extracted during the DNS simulations converges to the value predicted by the QSS model as Π_1 increases.

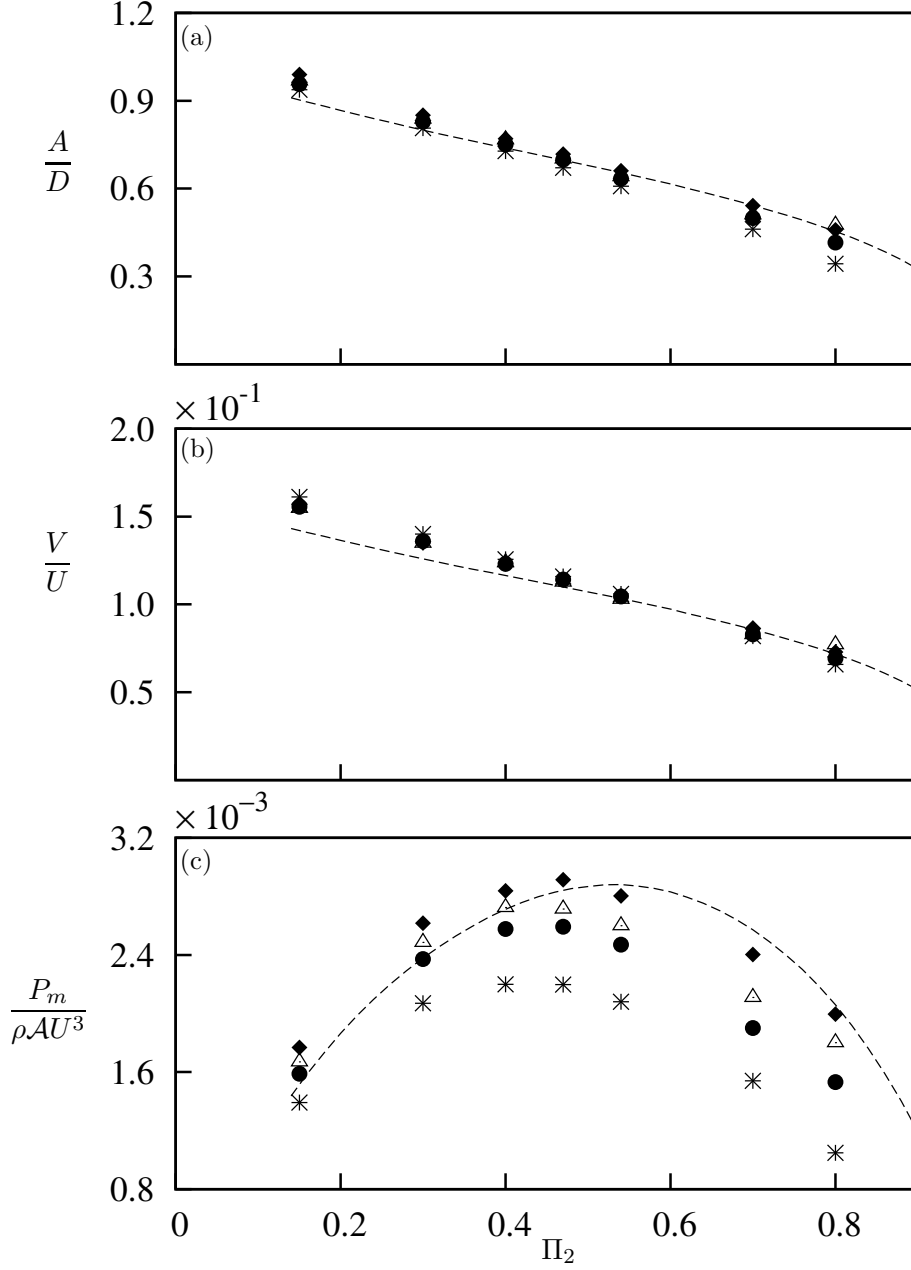


Figure 1.7: Comparison of data generated using the quasi-static model and full DNS simulations at (a) Displacement amplitude, (b) velocity amplitude and (c) dimensionless mean power as functions of Π_2 . Data were obtained at $Re = 200$ at four values $\Pi_1 = 10$ ($m^* = 20.13$) (*), $\Pi_1 = 60$ ($m^* = 49.31$) (●), $\Pi_1 = 250$ ($m^* = 100.7$) (△) and $\Pi_1 = 1000$ ($m^* = 201.3$) (◆). The QSS data at $\Pi_1 = 10$ (---).

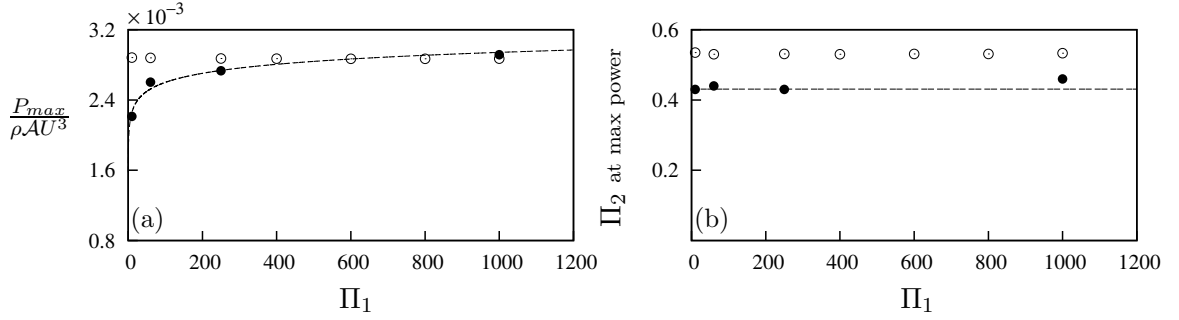


Figure 1.8: (a) Maximum power and (b) the value of Π_2 at maximum power of QSS data (○) and DNS data (●), as functions of Π_1 . For the DNS data, the maximum power asymptotes to an upper value with increasing Π_1 , while the value of Π_2 where maximum power occurs is relatively insensitive to Π_1 . The maximum power of the QSS data remains relatively constant, as does the value of Π_2 where maximum power occurs. The dash curve (---) of (a) follows the logarithmic fit of the maximum power which is $P_{max}/\rho AU^3 = 1.48 \times 10^{-4} \ln(\Pi_1) + 1.9 \times 10^{-3}$. The dashed curve in (b) shows the value $\Pi_2 \simeq 0.43$.

Figure 1.8(b) shows the value of Π_2 at which the turning point, and therefore the maximum power output, occurs. The open symbols show the value predicted by the QSS model, the closed symbols show the value predicted by the DNS. The two are not the same, with a value around 0.41 predicted by the DNS (shown with a dashed line) and a value above 0.5 predicted by the QSS model. However, both models show that while the power extracted is a reasonably strong function of Π_1 , the value of Π_2 at which this maximum power occurs is relatively unaffected.

In an effort to further quantify the performance of the QSS model, the percentage between the QSS and DNS extracted power data as a function of Π_1 was calculated using the equation

$$\% \text{ error} = \left| \frac{P_{m(QSS)} - P_{m(DNS)}}{P_{m(DNS)}} \right| \times 100. \quad (1.9)$$

The results of this calculation are plotted in figure 1.9, along with a power-law best fit $138.697\Pi_1^{-0.6}$. The figure clearly shows that as Π_1 increases, the error between the QSS and DNS models quickly decreases. However, at low values of Π_1 , the discrepancy between the two can be quite large, around 30%.

A likely reason for this discrepancy at low Π_1 is the influence of the vortex shedding,

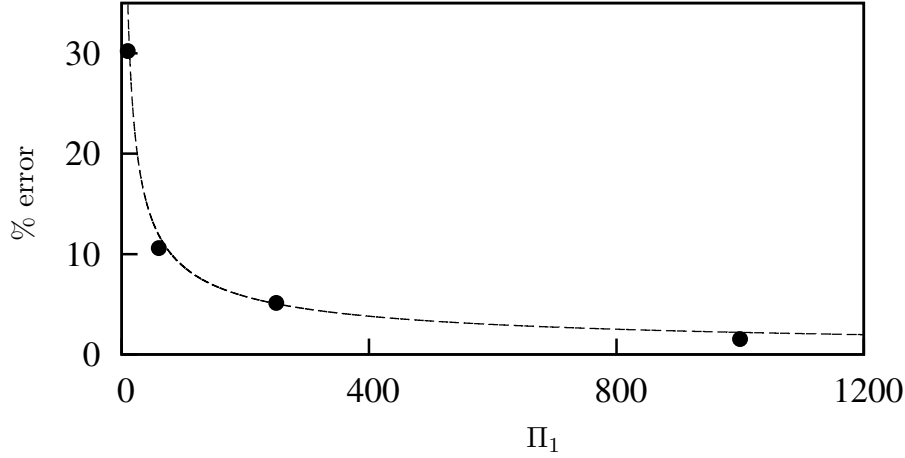


Figure 1.9: The percentage error between the maximum power obtained using DNS data and predicted by QSS model as a function of Π_1 . The deviation between them is large for low values of Π_1 . The dash curve (---) follows the power law fit of the percentage error which is $\%error = 138.697\Pi_1^{-0.6}$.

which is not accounted for in the QSS model. To investigate this further, frequency spectra for the body velocity from DNS cases at varying values of Π_1 , at a value of $\Pi_2 = 0.47$ (close to the value at which the mean extracted power is a maximum), have been produced. They are presented, along with the original time histories in figure 1.10.

This figure shows the velocity signals at $\Pi_1 = 0.8$ and $\Pi_2 = 10, 60, 250$ and 1000 and the corresponding spectrum. The spectral data shows a significant frequency component around $fd/U = 0.156$ which can be identified as the vortex shedding frequency. The magnitude of the frequency component at the vortex shedding frequency clearly reduces as Π_1 is increased. This indicates that the influence of vortex shedding is much more prominent at low Π_1 , therefore resulting in larger deviations from quasi-steady state results. This builds on the work of Joly et al. (2012), which was conducted at zero damping, that implied that mean extracted power would be influenced by vortex shedding at low mass.

This influence is explicitly shown here. Figure 1.11 plots the relative intensity of the component at the vortex shedding frequency to the component at the galloping or oscillation frequency in the spectra of figure 1.10.

Similar to the discrepancy between the QSS and DNS mean extracted power shown in figure 1.9, the relative strength of the vortex shedding is seen to be large at small values

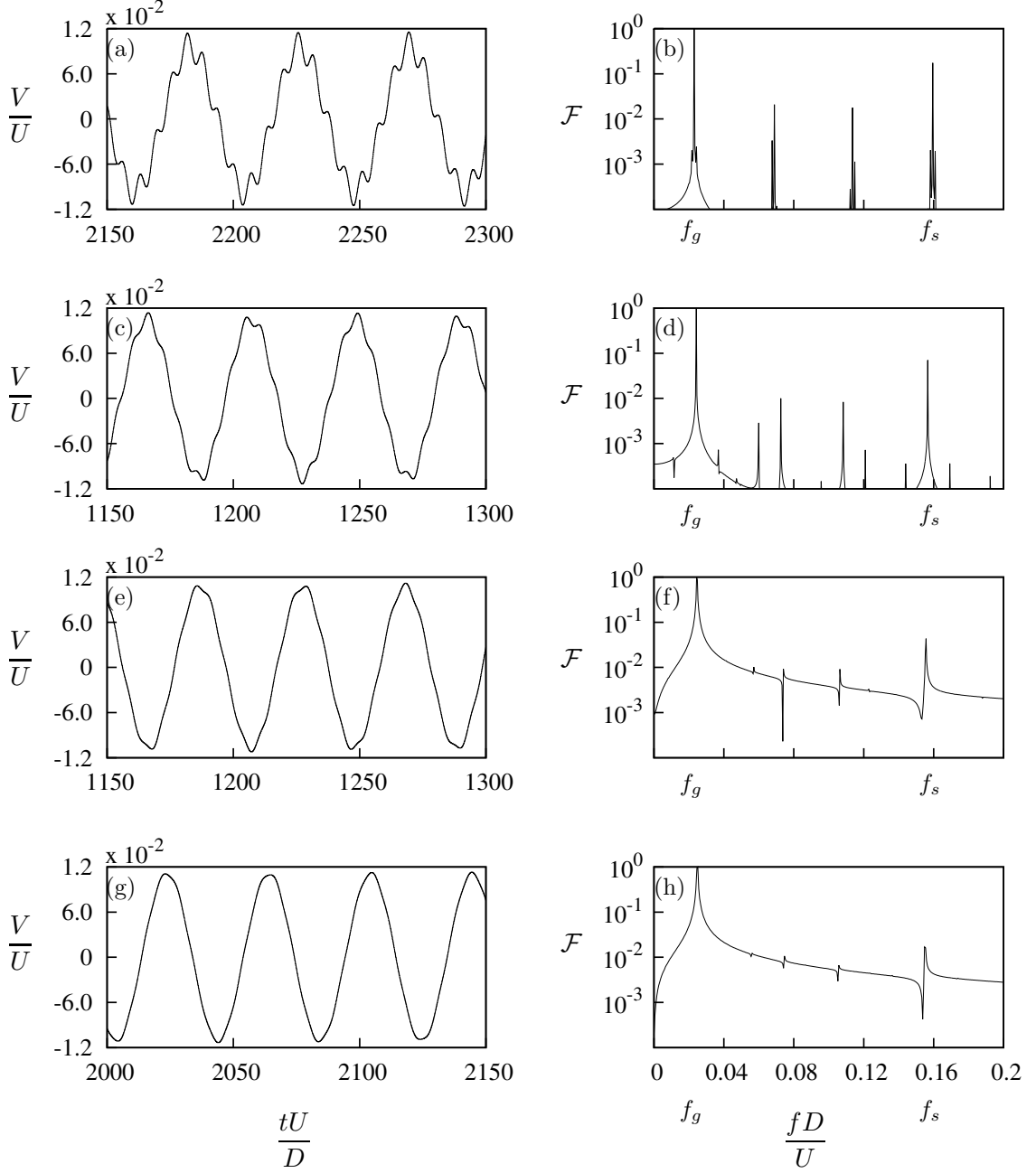


Figure 1.10: Velocity signal (right) and the corresponding power spectrum (left) of the DNS data at four values of Π_1 at $\Pi_2 = 0.47$. (a) and (b) $\Pi_1 = 10$, (c) and (d) $\Pi_1 = 60$, (e) and (f) $\Pi_1 = 250$, (g) and (h) $\Pi_1 = 1000$. f_g and f_s represents galloping and vortex shedding frequencies respectively. U^* is kept at 40 therefore the mass ratio increases as Π_1 increases. It is evident that the influence of vortex shedding reduces as the inertia of the system increases.

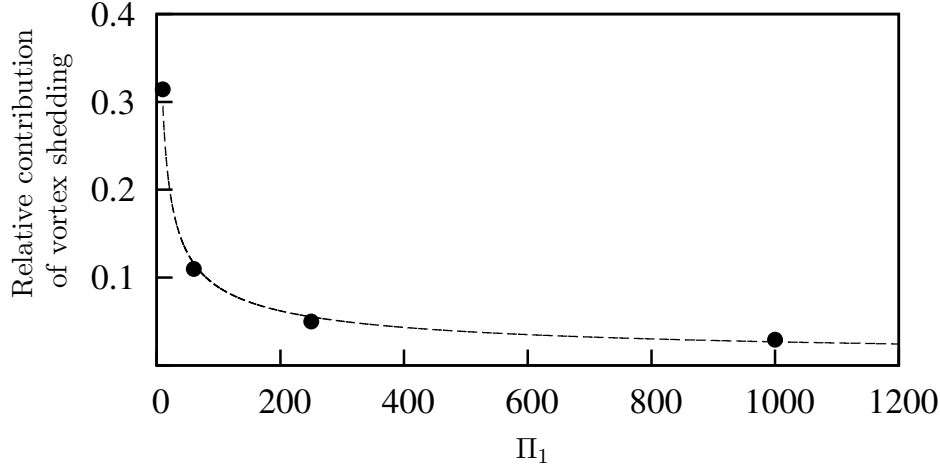


Figure 1.11: The relative power of the vortex shedding as a function of Π_1 . The relative power of the vortex shedding decreases as Π_1 increases. The dash curve (---) follows the power law fit of the percentage error which is $\text{Relative power} = 0.977\Pi_1^{-0.52}$.

of Π_1 , and quickly decreases as Π_1 is increased. The figure shows that the relative power of the vortex shedding frequency to the galloping frequency varies like $0.977\Pi_1^{-0.52}$.

The difference between the power predicted by the QSS and DNS models scales with $\Pi_1^{-0.6}$; the relative power at the vortex shedding frequency scales with $\Pi_1^{-0.52}$. These scalings are quite similar, and both are close to $1/\sqrt{\Pi_1}$. While not unequivocal, this correlation strongly indicates this discrepancy is due to the influence of the vortex shedding, even though the vortex shedding and galloping frequencies remain separated by around the same amount for all values of Π_1 presented in figure 1.10. The data presented in figure 1.11 also give some indication of the strength of any vortex shedding correction term that might be added to the QSS model in an effort to decrease the discrepancy between it and the DNS simulations.

Further information can be gained by observing the flow field. Non-dimensionalised flow field data at values of Π_2 close to where maximum power is produced at different Π_1 are presented in figure 1.12. The figure shows a clear wavelength of the wake as Π_1 is increased. Qualitatively, this can be interpreted as showing that at high Π_1 , the vortex shedding is simply superimposed over the path of motion of the cylinder. It shows a decrease in amplitude of the path of the body at low Π_1 , which may be due to the higher levels of non-linear interaction between the vortex shedding and galloping. Such an argument is

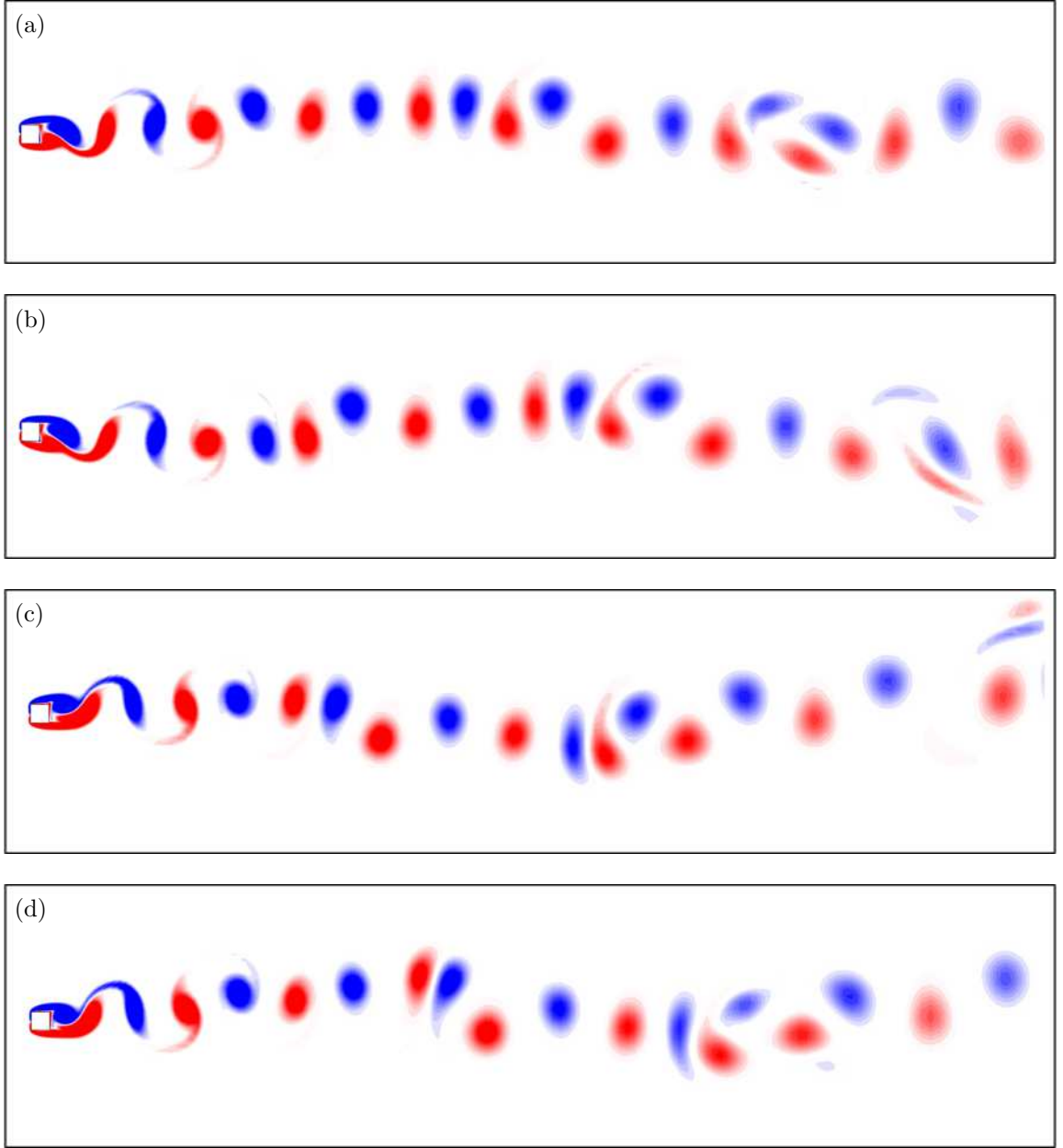


Figure 1.12: Vorticity plots of the flow at arbitrary instants at $\Pi_2 = 0.47$. (a) $\Pi_1 = 10$, (b) $\Pi_1 = 60$ (c) $\Pi_1 = 250$ and (d) $\Pi_1 = 1000$ at $Re = 200$. Contours show vorticity at levels between ± 1 .

consistent with the data of figure 1.11 that show the increasing influence of vortex shedding on the velocity of the body as Π_1 decreases. Taken together, this also goes some way to explaining the discrepancy between the output power predicted by the QSS and DNS

models at low Π_1 , highlighted in figure 1.9.

1.1 Summary of the governing parameters of fluid-elastic galloping

A need arose after the literature survey to obtain suitable scaling parameters for galloping. These parameters Π_1 and Π_2 , were formulated through the natural time-scales of the linearised Quasi-steady state model.

The power transfer of a square body under fluid-elastic galloping was analysed by solving the quasi-steady state oscillator model equation using numerical integration. Power data were analysed for both traditional VIV and the newly formulated scaling parameters. A good collapse for predicted output of power could be obtained using the newly formulated dimensionless groups (Π_1 , Π_2) in comparison with the classical VIV parameters ,i.e., ζ and U^* . The collapsed data using the dimensionless groups strengthens the argument that the velocity amplitude and the power transfer of the system does not depend on the natural frequency of the system over a large range of natural frequencies.

Even though m^* is an independent parameter as shown in equation 1.8, the results showed that the system is essentially a function of Π_1 and Π_2 only. This seems to be explained by inspection of equation 1.8, which shows that m^* only has an impact on the forcing terms which are non-linear in relation to the body velocity. For these terms to be appreciable, the velocity of the body (and therefore the induced angle of attack) needs to be very high, which appears not to be the case for the range of parameters tested here.

In comparison with the direct numerical simulation data, it could be concluded that the QSS model provides a good estimate of the power output of the system when Π_1 is relatively high. However, at low values of Π_1 , the prediction is not close due to the fact that the QSS model does not account for the influence of vortex shedding which is shown to increase as Π_1 is decreased. However, the QSS model does provide a reasonable prediction of the value of Π_2 at which maximum power is produced. Both the error in predicted maximum power between the QSS and the DNS models, and the relative power of the vortex shedding, have been quantified and scale similarly to $1/\sqrt{\Pi_1}$.

BIBLIOGRAPHY

- Barrero-Gil, A., Alonso, G., Sanz-Andres, A., Jul. 2010. Energy harvesting from transverse galloping. *Journal of Sound and Vibration* 329 (14), 2873–2883.
- Barrero-Gil, A., Sanz-Andrés, A., Roura, M., Oct. 2009. Transverse galloping at low Reynolds numbers. *Journal of Fluids and Structures* 25 (7), 1236–1242.
- Bernitsas, M. M., Ben-Simon, Y., Raghavan, K., Garcia, E. M. H., 2009. The VIVACE Converter: Model Tests at High Damping and Reynolds Number Around $10^{[sup 5]}$. *Journal of Offshore Mechanics and Arctic Engineering* 131 (1), 011102.
- Bernitsas, M. M., Raghavan, K., Ben-Simon, Y., Garcia, E. M. H., 2008. VIVACE (Vortex Induced Vibration Aquatic Clean Energy): A new concept in generation of clean and renewable energy from fluid flow. *Journal of Offshore Mechanics and Arctic Engineering* 130 (4), 041101–15.
- Bouclin, D. N., 1977. Hydroelastic oscillations of square cylinders. Master’s thesis, University of British Columbia.
- Joly, A., Etienne, S., Pelletier, D., Jan. 2012. Galloping of square cylinders in cross-flow at low Reynolds numbers. *Journal of Fluids and Structures* 28, 232–243.
- Lee, J., Bernitsas, M., Nov. 2011. High-damping, high-Reynolds VIV tests for energy harnessing using the VIVACE converter. *Ocean Engineering* 38 (16), 1697–1712.
- Leonard, A., Roshko, A., 2001. Aspects of flow-induced vibrations. *Journal of Fluids and Structures* 15, 415–425.
- Luo, S., Chew, Y., Ng, Y., Aug. 2003. Hysteresis phenomenon in the galloping oscillation of a square cylinder. *Journal of Fluids and Structures* 18 (1), 103–118.

BIBLIOGRAPHY

- Parkinson, G. V., Smith, J. D., 1964. The square prism as an aeroelastic non-linear oscillator. *The Quarterly Journal of Mechanics and Applied Mathematics* 17 (2), 225–239.
- Raghavan, K., Bernitsas, M., Apr. 2011. Experimental investigation of Reynolds number effect on vortex induced vibration of rigid circular cylinder on elastic supports. *Ocean Engineering* 38 (5-6), 719–731.
- Shiels, D., Leonard, A., Roshko, A., 2001. Flow-induced vibration of a circular cylinder at limiting structural parameters. *Journal of Fluids and Structures* 15, 3–21.
- Vicente-Ludlam, D., Barrero-Gil, A., Velazquez, A., 2014. Optimal electromagnetic energy extraction from transverse galloping. *Journal of Fluids and Structures* 51, 281–291.
- Vio, G., Dimitriadis, G., Cooper, J., Oct. 2007. Bifurcation analysis and limit cycle oscillation amplitude prediction methods applied to the aeroelastic galloping problem. *Journal of Fluids and Structures* 23 (7), 983–1011.